Original Article

Evidence of lithium mobility under neutron irradiation

Xiao-Ying Yu [a,*], *Jennifer Yao* [a], *Bethany Matthews* [a],
Steven R. Spurgeon [a], *Shawn Riechers* [a], *Gary Sevigny* [a], *Zihua Zhu* [b],
Weilin Jiang [a], *Walter Luscher* [a,**]

[a] *Energy and Environment Directorate, Pacific Northwest National Laboratory, Richland, WA, 99352, USA*
[b] *W.R. Wiley Environmental Molecular Science Laboratory, Pacific Northwest National Laboratory, Richland, WA, 99352, USA*

ARTICLE INFO

ABSTRACT

Understanding compositional and microstructural changes in functional intermetallic coatings is of great importance for fusion energy and nuclear materials applications. Tritium (^{3}H) and lithium (^{6}Li, ^{7}Li) transport within a neutron irradiated target rod employing an aluminide-coated austenitic stainless-steel cladding was investigated using state-of-the-art multimodal imaging. Specifically, a scanning electron microscope augmented with focused ion beam (SEM-FIB) was used to prepare lift-out samples of the irradiated coating for micro-analysis. Scanning transmission electron microscopy (STEM) was used to acquire atomic-scale information on the coating surface microstructure, morphology, and composition. Atomic force microscopy (AFM) was used to determine lift-out dimensions nondestructively. Time-of-flight secondary ion mass spectrometry (ToF-SIMS) revealed the presence of carbonaceous species and unexpected lithium isotopic distributions in the irradiated tubing, suggesting light isotope mobility between internal target components during irradiation. SIMS chemical mapping of aluminide coatings at core midplane and lower core locations of the cladding shows that light isotopic (e.g., ^{3}H, ^{6}Li, ^{7}Li) distributions are different in the irradiated coating. Advance correlative imaging results suggest lithium transport during the tritium production process and give new insights into the fundamental transport mechanism within the target during irradiation and non-equilibrium conditions.

© 2021 The Author(s). Published by Elsevier B.V. This is an open access article under the CC BY-NC-ND license (http://creativecommons.org/licenses/by-nc-nd/4.0/).

1. Introduction

Iron aluminide, Fe–Al alloys with about 20–50 at. % Al are among the most widely studied intermetallic compounds due to their oxidation and wear resistance, low density, and economical cost compared to steels. Although the use of bulk iron aluminide is limited due to relatively poor low temperature ductility and poor high temperature creep resistance, its coatings are frequently utilized to protect steel substrates [1–4]. Surface characterization techniques are often used to

---

interrogate thin coatings and deposits of iron aluminide [5,6]. Many techniques including electron microscopy, imaging, and depth/surface profiling spectroscopy are used [7]. Scanning electron microscopy (SEM) is a popular choice to characterize iron aluminide coating [8–13]. For example, the intermetallic character and mechanical properties of iron aluminide was elucidated using SEM [14–16]. Another attractive approach is transmission electron microscopy (TEM) [17–24]. Time-of-flight secondary ion mass spectrometry (ToF-SIMS) offers sensitive mapping of elements, isotopes, and molecules with submicrometer spatial resolution, which makes this an attractive technique among the known tools used in iron aluminide characterization [25]. One unique capability of SIMS is that it can be used to characterize hydrogen isotopes [26–28], this capability is not available in other microscopy and microanalysis, such as SEM, TEM, or optical microscopy. However, its use in coating characterization is not as widespread compared to electron microscopy [29,30]. Advancements in microanalysis and microscopy in the past decade have made it possible to study irradiated materials with much improved spatial resolution. SEM–FIB, scanning transmission electron microscopy (STEM), atomic force microscopy (AFM), and ToF-SIMS were chosen to validate the hypotheses and demonstrate the feasibility of studying irradiated materials in ways that were previously impossible.

Hydrogen isotope production can be achieved by irradiating materials or targets with specified isotopic compositions using neutron irradiation. Target constituent isotopes are consumed during irradiation through various nuclear processes, such as neutron capture and decay, producing a desired isotope. Target materials are typically held within irradiation vehicles designed to accommodate the irradiation environment and often include features that ensure successful containment and recovery of the isotope produced by the target material. The $FeAl_3$ coating investigated in this work is part of a tritium breeding target [31]. A stack of annular, ^6Li-enriched lithium aluminate ($LiAlO_2$) pellets is contained within an austenitic Type 316 stainless steel (316SS) cladding tube. Tritium is produced in the pellet stack via the following reaction $^6Li+(n)\rightarrow 4He+^3H$. The pellet stack is surrounded by a series of concentric tubes that catalyze a variety of surface reactions including hydrogen reduction and sorption.

Aluminum-rich phases (>16–18 at%), like $FeAl_3$, provide a protective surface layer of aluminum oxide that offers enhanced oxidation resistance and forms an effective hydrogen diffusion barrier [1,32,33], making them frequent candidates for specialized applications [3,18]. This was the driver for depositing an aluminide barrier on the inner diameter of the 316SS TPBAR cladding tube. However, the influence of irradiation on the surface chemistry and structure of the aluminide coating at the microscale is not well established. In addition, surface discoloration of the aluminide coating observed during post irradiation examination indicates that carbonaceous compounds may be deposited during irradiation. There is carbon impurity in the pellets, likely contributing to the carbon content [34]. Co-deposition of carbon and hydrogen isotopes and deposition of hydrogenate carbon radicals and molecules are a known process for tritium retention in the tritium barrier surface [35]. Moreover, we investigate the potential gas diffusion of lithium and tritium under elevated

temperature post irradiation examination (PIE), not solid-state diffusion. Post-irradiation characterization of this deposit and the aluminide coating is expected to provide additional insight regarding compositional and structural changes in-service. Knowing the chemical composition of the surface deposits will provide new insights into the transport of light elements and isotopes within the tritium barrier device. Advanced correlative chemical imaging builds a stronger technical base of material transport and such information is crucial to improve our fundamental understanding of material transport under neutron irradiation and at non-equilibrium conditions.

The iron aluminide coating evaluated in this study was used as a diffusion barrier on a Type 316SS tube to mitigate the permeation of tritium (^3H), an isotope of hydrogen, from an isotope producing target [31]. The targets were irradiated for approximately 500 days and the temperature of the iron aluminide-coated cladding was about 300 °C. During PIE, black deposits were observed in isolated locations on the stainless-steel tube. These observations were made near the bottom of the target where gaps between target components permit gas communication between the target material and the $FeAl_3$ diffusion barrier. Concerns over the potential impact of these deposits on the functionality of the coating prompted a need for surface deposit chemical characterization.

The potential reaction between the deposit and coating should be mitigated by a protective alumina barrier on the coating surface. The possible existence of the carbonaceous deposit on the iron aluminide coating leads to the hypothesis that tritium may be transported by carbon compounds and deposit on the top of the coating during irradiation; thereby by eluding the components designed for hydrogen sorption. Additionally, Li isotopes, ^6Li and ^7Li, may become mobile during tritium production under elevated temperature. Volatile organic compounds are known to form via radical induced chain reactions in the gas phase. These products may participate in the transport of lithium species. The high temperature and irradiation conditions could potentially contribute to the carbonaceous deposit formation on the aluminide coating [36–39]. However, the analysis of irradiated coating materials can be difficult due to the radiological hazards posed to the operator and the instrument. Other complications include the fact that all surfaces everywhere are covered in carbon and distinguishing environmental carbon from carbon deposited during irradiation is very difficult using traditional surface analysis methods such as X-ray photoelectron spectroscopy (XPS).

2. Materials and methods

2.1. Sample selection

A representative target rod was selected in accordance to previous reports [31]. The irradiated tube was sectioned to produce a full-round sample (Figs. S1 and S2b). One-eighth of the full-round sample was used to prepare multiple SEM-FIB lift-out samples (Fig. S2c). Irradiated tube samples from the lower core region and core midplane, approximately 2 m apart during irradiation were used to investigate possible transport of lithium isotopes along the length of the target rod.

2.2. SEM-FIB

Multiple lift-out samples for STEM, AFM, and ToF-SIMS were prepared on a Thermo Fisher Helios Dual Beam 660 FIB microscope [40–43]. Standard cross-sectional TEM lift-out methods were used for the STEM samples with the ion beam at 30 kV, followed by attachment with Pt to a TEM grid. A Mo grid was used as tritium tends to soak into Cu grids. Thinning of STEM samples were performed in the following: 30 kV at 56–57° tilt, 16 kV at 54° tilt, 8 kV at 53.5° tilt, and 5 kV at 54° tilt. Reducing the angle in steps as the accelerating voltage lowered was used to minimize FIB damage. Final polishing was performed at 2 kV ion milling energy and 59° tilt. A thin layer to Pt was coated onto the cladding surface to protect the surface before performing the lift-out process for ToF-SIMS samples. When multiple lift-out samples were used, they were chosen close to each other in the irradiated cladding. ToF-SIMS steel cladding samples were prepared at a reduced size of 10 μm × 10 μm × 4 μm to conform with radiological control requirements. These samples were first coated with 300 nm of Pt to protect the surface from the ion beam. They were then cut out with a trenching pattern, similar to the preparation of the TEM sample. However, the undercut was performed from both sides with a stage tilt of 22°, making a wedge at the bottom. The lift-out was then welded with Pt to the center of a clean Si wafer prior to AFM and ToF-SIMS analyses.

2.3. STEM

High-angle annular dark field (STEM-HAADF) images were collected on a JEOL ARM-200CF microscope operating at 200 kV, with a convergence semi-angle of 27.5 mrad and an inner collection angle of 68 mrad. STEM energy-dispersive X-ray spectroscopy (STEM-EDS) maps were collected using a JEOL Centurio detector setup, with a 1 Å probe size, ~120 pA probe current, 10 μs px^{-1} dwell time, and 5–10 min total acquisition time.

2.4. AFM

Height profiles of the SEM-FIB lift-out samples were measured by an MFP-3D Infinity (Asylum/Oxford) atomic force microscope. Tapping mode measurements were performed using a soft cantilever (AC240TSA-R3, Asylum, 2 N/m spring constant) with a set point of 3 V, a drive amplitude of 190 mV, and a scan speed of 0.3 Hz. The image was leveled using the flat portion of the substrate (omitting the FIB section and scratches) which was used as a baseline to determine the average height of the lift-out plateau.

2.5. ToF-SIMS

ToF-SIMS V spectrometer (IONTOF, GmbH, Münster, Germany) was used for spectral analysis and depth profiling. Surface mapping of unirradiated cladding samples was acquired in the static mode. 25 keV Bi$^+$ was used as the analysis beam, and data were collected in both negative and positive ion modes. The mass spectrometer mode was used to acquire spectra with high mass resolution for 60 scans. All spectra were mass calibrated using CH^-, OH^-, and CN^- for the negative ions and CH_2^+, CH_3^+, $C_3H_3^+$ for the positive ions. Measurement reproducibility of unirradiated cladding is illustrated in Fig. S4. Additional spectral results are depicted in Figs. S6 and S7.

The dynamic depth profiling of the unirradiated and irradiated cladding lift-out samples were also performed. Negative secondary ion depth profiling was suitable for $^3H^-$ detection because H^- was more sensitive than H^+. Additionally, H_2^- and H_3^- interferences were weak in the negative mode. Additional H depth profiling and experimental details have been described in our previous publications [26,27]. In brief, dual beam depth profiling mode was used. A 2 keV Cs$^+$ beam was used as the sputter beam and the 25 keV Bi$^+$ beam was used as the analysis beam. The Cs beam rastered over a 200 μm × 200 μm surface for sputtering and Bi$^+$ rastered over a 50 μm × 50 μm area for analysis. Depth profiles were acquired using the non-interlaced mode to reduce the charging effect in addition to applying the 10-eV electron flood gun. The raster size of mass spectra, depth profiles, and images was set to 128 × 128 pixels. Data were collected in the negative ion mode ranging from 650 to 750 scans during depth profiling. The entire depth profile of the irradiated bottom cladding is shown in Fig. S8.

2.6. Correlative chemical imaging of irradiated cladding

Fig. 1 depicts sample preparation and the multimodal imaging workflow employed in this work. These techniques give rich, complementary information of the same regions of a sample in a way that area-averaged (e.g., x-ray or neutron-based) techniques could not offer, especially on activated materials. Specifically, micrometer-sized irradiated cladding samples were prepared using SEM-FIB to reduce radiological exposure to the analytical instrument and the operator (Fig. 1b). STEM was used to reveal the nanostructure in the suspected carbonaceous deposit (Fig. 1c). ToF-SIMS was used to gain significant insights regarding the condition of engineered coating in this work. Of particular interest to the carbonaceous deposit and coating materials, ToF-SIMS provides three-dimensional (3D) chemical mapping of the material using depth profiling, thus giving a vivid visualization of the light isotope distribution within the deposit layer that is postulated to form due to irradiation and heating (Fig. 1e). AFM (Fig. 1d) is a nondestructive imaging method. It was used to complement SEM and ToF-SIMS imaging.

Irradiated SEM-FIB lift-out samples from the cladding near the midplane and near the bottom of the reactor core were selected for multimodal imaging to investigate the hypotheses. AFM (Fig. 1c and Fig. S3) was used to verify the crater depth of ToF-SIMS depth profiling and determine the thickness of the surface materials being analyzed. Since the depth profiling sputtering rate of different materials varies in ToF-SIMS [44–48], AFM provides a reliable physical measurement of the crater depth before and after the depth profiling and ensures the depth measurement accuracy [49]. STEM and ToF-SIMS were used to obtain the most needed information of morphological and chemical changes and investigate the hypotheses. However, STEM could not detect light elements such as ^3H and Li as well as ToF-SIMS.
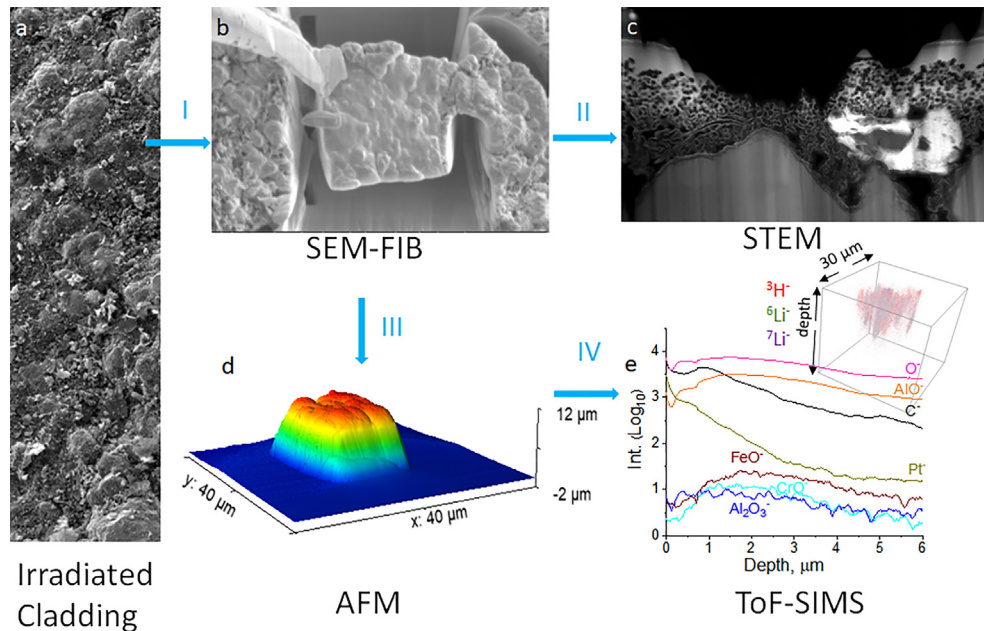
Fig. 1 – Multimodal chemical imaging of an irradiated tube (a) using (b) SEM-FIB to prepare the lift-out, (c) STEM to determine nanostructures and elemental mapping, (d) AFM to obtain the lift-out dimensions nondestructively, and (e) ToF-SIMS to acquire sensitive surface and isotopic, elemental, and molecular 3D mapping.

3.   Results and discussion

3.1.   Determination of the carbonaceous deposit

To study the surface condition of the iron aluminide layer, STEM and ToF-SIMS were performed. Fig. 2 shows energy-dispersive x-ray spectroscopy (STEM-EDS) maps of the irradiated bottom cladding sample, revealing a rough surface morphology (Fig. 2b). The formation of a clear 50—60 nm aluminum oxide layer on the surface was observed (Fig. 2c-d), as well as a thick carbon network consisting of porous, chain-like structures on the surface. The oxide layer is uniform and present throughout the entire imaging region, while the carbon network is more irregular (Fig. 2b-c). The latter is also only present in the irradiated sample. The STEM imaging findings show that a carbonaceous deposit indeed forms on the coating surface following irradiation.

3.2.   Evidence of Li transport during irradiation

ToF-SIMS was used to provide more in-depth analysis of the carbonaceous deposit composition and spatial distribution in addition to STEM's elemental and morphological mapping.
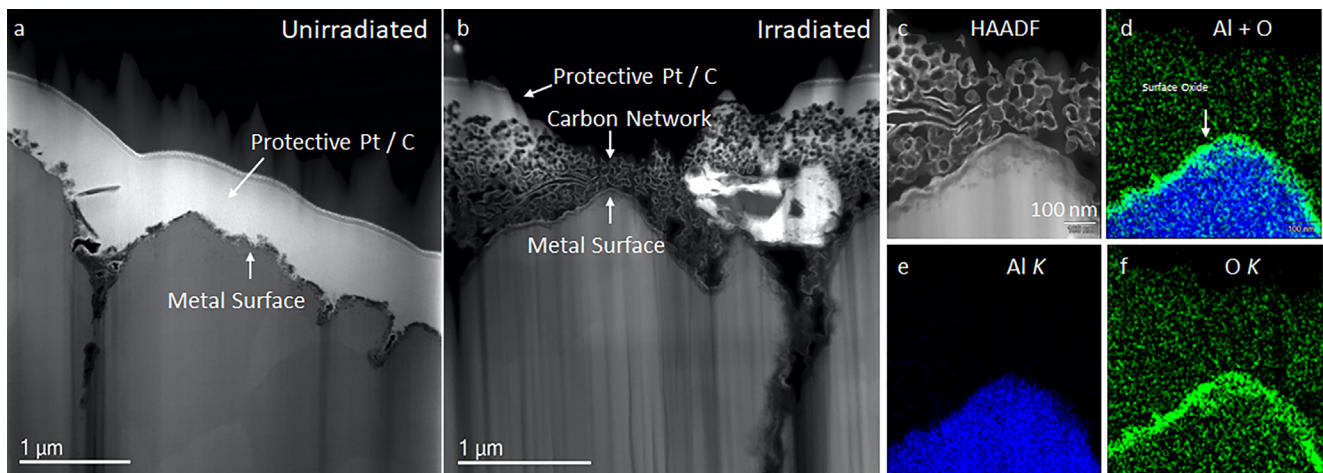

Fig. 2 – Representative cross-sectional STEM-EDS maps of the unirradiated cladding (a), irradiated cladding (b), closeup high-angle annular dark-field (HAADF) STEM images of the porous carbon network (c), and elemental mapping of Al (blue) and O (green) (d), Al (e), and O (f) in the irradiated cladding showing the presence of a surface oxide layer.

Two types of SIMS measurements were performed, high mass resolution spectral analysis and depth profiling. Measurement reproducibility was illustrated in Figs. S4a–b.

Table 1 gives a summary of key peaks identified in the ToF-SIMS spectral analysis. Interestingly, m/z^- 101.9 alumina (AlR_2ROR_3R) signal is observed in the pristine unirradiated iron aluminide cladding (Fig. S4a) [53], complementing the elemental maps shown in Fig. 2. Iron aluminide coatings are often made by applying Al slurries followed by a diffusion heat treatment at 650 °C. These coatings enhance the resistance of both ferritic and austenitic steel to steam oxidation at the same temperature for over a long time [54]. Although the presence of alumina was suspected as one of the byproducts of the powdered coating approach used to engineer the iron aluminide coating as the tritium barrier, the evidence of its existence was yet to be found until the STEM and ToF-SIMS imaging results reported in this work. The existence of alumina is determined unambiguously, because ToF-SIMS gives molecular detection (Fig. S4a).

Irradiated cladding samples were analyzed in detail to study the hypothesis of tritium deposition, the source of carbon compounds, and possible lithium transport under irradiated conditions. Fig. 3 depicts ToF-SIMS spectral comparison of the irradiated bottom cladding, irradiated middle cladding of the same tube, and an unirradiated cladding as control. ToF-SIMS gives sensitive detection of the material interfaces of both unirradiated and irradiated coated tubes, with detailed chemical spatial distribution. A key observation is that tritium ($^3H^-$) was observed in both the irradiated core midplane and lower core samples (Fig. 3a-b) but not in the unirradiated control (Fig. 3c). The inserts of each spectrum on the left in Fig. 3 show that $^3H^-$ m/z^- 3.0167, $^2H^1H^-$ m/z^- 3.0226, and H_3^- m/z^- 3.0244 are distinctive, giving confidence in the observation. The ratio of the $^3H^-$ count to that of $^1H^-$ is 0.015, significantly higher than the natural isotopic abundance [55]. Thus, SIMS spectral observations indicate that the tritium deposited on the cladding coating is most likely a reaction product formed during irradiation. Data was collected from the selected depth of several micrometers where counts of $^3H^-$ and $^1H^-$ were stable.

In addition, C^3H^- m/z^- 15.0167, is observed in the irradiated lower core sample as a fragment of tritiated hydrocarbon (Fig. 3). Interestingly, the peak intensity of C^3H^- is much higher than CH_3^- in the irradiated tube surface as depicted in the inserted spectra on the right in Fig. 3. In contrast, the peak of C^3H^- m/z^- 15.0167 is not observed in the unirradiated SIMS spectrum. The two prominent peaks are NH^- m/z^- 15.0114 and CH_3^- m/z^- 15.0240 in the latter. This spectral comparison shows that the tritiated hydrocarbon compounds are products of neutron irradiation. Additionally, the fact that the tritiated hydrocarbon fragment has much higher counts than those of the hydrocarbon fragment suggests that hydrogen isotopic exchange reactions are quite dominant in tritium processing. The finding of the tritiated products in the coating surface indicates tritium transfer and deposit in the aluminide coating under elevated temperature and irradiation. Some of the tritium that is present as a hydrocarbon suggests that chemical processes and isotopic exchange have taken place due to irradiation.

Industrial tritium production mainly consists of tritiated water $^1H^3HO$ and hydrogen $^1H^3H$, and tritiated methane ($C^1H_3^3H$). For example, tritiated methane is a typical hydrocarbon in tritium production that can be produced from reactions of tritium and hydrocarbons. The observation of C^3H^- m/z^- 15.0167 as a fragment of tritiated hydrocarbon suggests that they may come from reactions of deposited tritium at the iron aluminide coating [56]. Hydrogen isotope exchange reaction by β-radiation of tritium has been studied [57–60]. Hydrogen radicals have a long lifetime in hydrogen isotopes mixed gas. However, methane is found to scavenge these radicals in the methane mixed gas to form tritiated hydrocarbon even as an impurity in the reactor [61].

When comparing the two irradiated tube samples, only the sample from near the lower end of the core shows detection of $^6Li^-$ $m/z=6.0157$ and $^7Li^-$ $m/z=7.0165$. The count ratio of $^6Li^-$:$^7Li^- = 0.206$ is much higher than the natural abundance of ^6Li:$^7Li = 0.0818$ [62]. The ratio of ^6Li to ^7Li was 0.3528 in the pellets before irradiation. This ratio is expected to be reduced to approximately half of the original value after irradiation [63]. The observed ratio of $^6Li^-$ to $^7Li^-$ in the aluminide coating surface suggests ^6Li and ^7Li are transported with equal preference from the irradiated pellet. The reduced ratio of $^6Li^-$ to $^7Li^-$ also indicates a reasonable depletion of ^6Li during the reactor cycle. This finding gives supporting evidence that the enriched

Table 1 – Key peaks observed in the ToF-SIMS in the negative ion mode.

| Observed m/z	Theoretical m/z	Peak identification	References
1.0086	1.0083	H^-	This work
2.0149	2.0146	$^2H^-$	This work
3.0166	3.0167	$^3H^-$	This work
6.0157	6.0156	$^6Li^-$	This work
7.0165	7.0165	$^7Li^-$	Li et al., 2011 [50]
15.0112	15.0114	NH^-	This work
15.0165	15.0167	C^3H^-	This work
15.0264	15.0240	CH_3^-	This work
26.9842	26.9820	Al^-	Collinet-Fressancourt et al., 2013 [51]
42.9794	42.9770	AlO^-	Collinet-Fressancourt et al., 2013 [51]
101.9536	101.9483	$Al_2O_3^-$	Visbal et al., 2016 [52]
71.9380	71.9303	FeO^-	This work
67.9392	67.9359	CrO^-	This work
194.9725	194.9653	$^{195}Pt^-$	This work
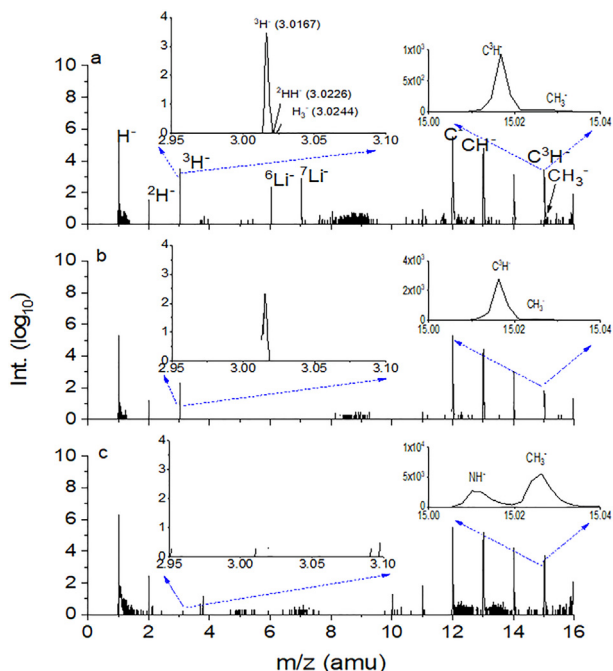
Fig. 3 – ToF-SIMS spectral comparison of (a) irradiated bottom, (b) irradiated middle, and (c) unirradiated cladding samples in the negative ion mode. The insert on the left shows the observations of $^3H^-$ in the irradiated cladding coating. The insert on the right shows the observed tritiated hydrocarbon C^3H^-peaks in the irradiated cladding coating.

$^6Li^-$ and $^7Li^-$ could become more mobile for transport to the aluminide barrier coating. Thus, the ToF-SIMS results give the spectral evidence to support our hypothesis regarding lithium mobility. The relationship between dose and the observed Li is not straightforward. There likely is no relationship between irradiation dose and Li concentration on the surface of the cladding. The selective deposition of Li at the bottom and not in the middle of the tritium barrier is entirely due to the configuration of the getter where there is a gas gap at the bottom, but not in the middle of the device. We only analyzed limited locations in one configuration of the tritium barrier in this work, it is not enough to make a generalized conclusion. More similar analysis is warranted to obtain a better understanding.

In addition, the depth profiling is important to rule out possible handling contamination in the hot cell. Otherwise, the Li profiles would be different at the surface. However, the question of how far the deposited tritium and carbon and migrated lithium may diffuse into the cladding remains unanswered. ToF-SIMS depth profiling measurements were performed to address this question. Fig. 4a–f depicts the comparison of depth profiling results of the irradiated core midplane and lower core samples against an unirradiated sample. The irradiated cladding lift-out samples were taken from locations suspected of deposition of carbonaceous materials. The cladding surface was protected using Pt coating before lifting out. The liftout dimension is 10 μm × 10 μm × 4 μm. Our results show that tritium migrates

into the iron aluminide coating that is approximately 80 μm thick [35] for several micrometers after irradiation compared to the unirradiated one. Particularly, there is significantly more $^3H^-$ in the lower core sample (Fig. 4a) within 3 μm compared to the core midplane sample (Fig. 4c). The finding of the gaseous diffusion of Li and ^3H at the bottom cladding is unexpected. The distributions of Li and ^3H track each other in the irradiated bottom cladding (Fig. 4a), suggesting that the diffusion may take place at the same time in the gas phase during high temperature irradiation. The fact that little tritium and no lithium are present in the midplane (Fig. 4b) indicates that the geometry at the bottom plane is central to the observed transport. The relationship between the gaseous diffusion of ^3H and Li is that the lithium diffusion is enhanced because of the tritium production process, in which ^6Li generates tritium and leads to the Li diffusion to other locations in the tritium barrier.

Potential lithium transfer during tritium production is a concern [28,64]. This new observation shows that tritium is also transported along the tube, favoring its adsorption on the cladding surface when there is a physical gap in the bottom [31]. The depth in Fig. 4 was estimated based upon the sputtering rate of 0.95 nm/s on a solid carbon reference using the same sputter setting in ToF-SIMS. Owing to the porous network structure of carbon shown in Fig. 2, the actual sputtering rate in this study is likely higher.

Equally interesting are the depth profiles of $^6Li^-$ and $^7Li^-$ in the cladding lift-outs. The depth profile of $^7Li^-$ m/z^- 7.0165 tracks that of FeO^- m/z^- 71.9380, $Al_2O_3^-$ m/z^- 101.9536, and CrO^- m/z^- 67.9392 well (Fig. 4a-b), suggesting that lithium is
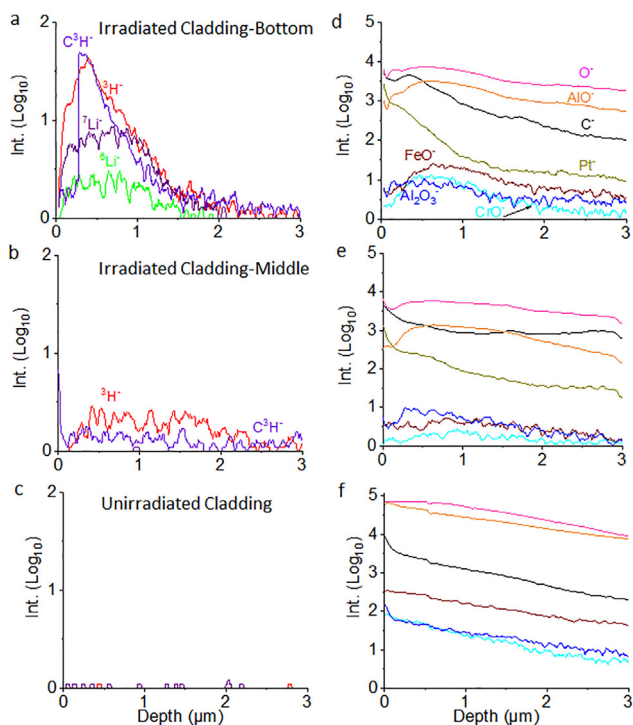

Fig. 4 – Comparison of ToF-SIMS depth profiles of key observed components of irradiated bottom cladding (a, b), irradiated middle cladding (c, d), and unirradiated cladding (e, f), respectively.
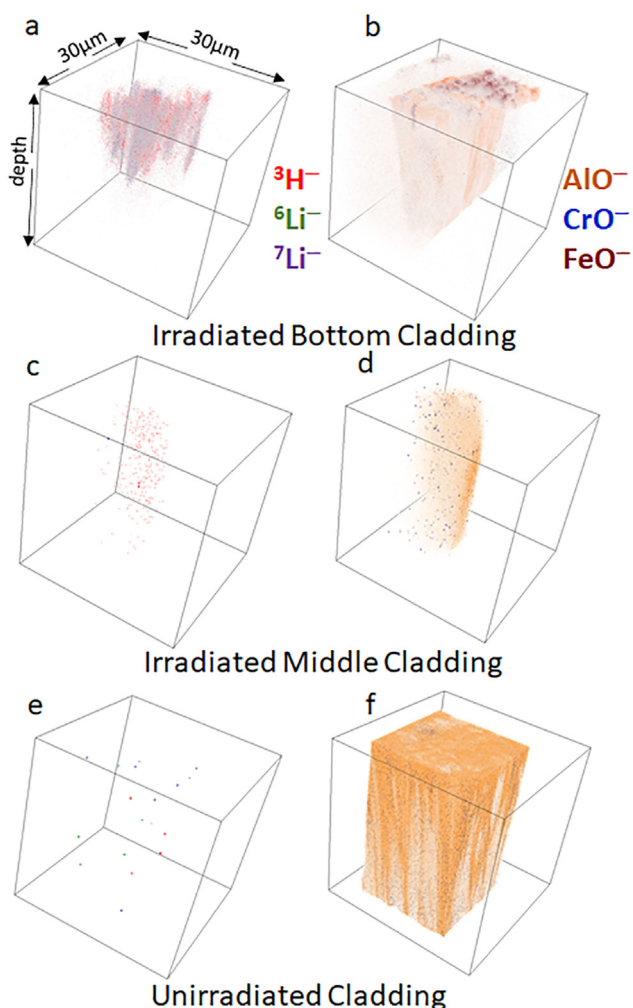
Fig. 5 — Comparison of reconstructed ToF-SIMS 3D images of selected characteristic ions in the irradiated bottom (a, b), middle (c, d), and nonirradiated (e, f) cladding samples, respectively.

Additionally, the difference in temperature of a couple hundred degrees between the two locations could play a role in tritium distribution.

Fig. 5a–5f shows the reconstructed 3D images of three selected ions relevant to tritium deposition and lithium transport, namely, $^3H^-$ m/z^- 3.0167, $^6Li^-$ m/z^- 6.0157, and $^7Li^-$ m/z^- 7.0165, corresponding to the depth profiles depicted in Fig. 4. There are more tritium and lithium isotopes deposited in the top few micrometers of the irradiated bottom cladding than the middle one as visualized in the 3D images (Fig. 5). These peaks are not present in the unirradiated cladding coating (Fig. 4e-f). Similarly, Fig. 5b, d, f show the reconstructed 3D images of three selected ions relevant to the composition of the aluminide coating AlO^- m/z^- 42.9794, other constituent CrO^- m/z^- 67.9392 related to Cr, and the stainless-steel component FeO^- m/z^- 71.9380. These components are conforming to the coating surface stoichiometry MAl_3, where M = Fe, Cr, Ni. Cr tends to diffuse more to the surface than Fe and Ni. These 3D images show that ToF-SIMS can uncover the unknown, affirm the known sensitively, and give vivid spatial distribution. Therefore, ToF-SIMS can be used to study materials undergone neutron irradiation, providing sub-micron chemical imaging of precious materials, and offering deeper insights into material processes involving extreme conditions such as irradiation and elevated temperature.

4.   Conclusions

Our findings show that sensitive surface technique offers new opportunities to probe the irradiated material interfaces, providing a unique atomic- and molecular-level insights lacking in previous studies. The novel multimodal approach has enabled previously inaccessible microanalysis for the characterization of carbonaceous surface deposits on irradiated iron aluminide coatings in this work and opened a new door to study nuclear materials and related material processing in the future. Of particular interest to understand tritium transport during irradiation, STEM imaging reveals the carbonaceous nanostructure. Combination of STEM elemental mapping via EDS and ToF-SIMS have, for the first time with our aluminide coating, revealed the presence and thickness of the oxide coating that was inferred to be present. Utilizing the correlative imaging workflow to study the irradiated cladding components among SEM/FIB, AFM, and ToF-SIMS allows us to discover that lithium could become mobile and transport along with tritium in the gas phase during tritium production. Consequently, we provide new insights regarding tritium adsorption and migration into the iron aluminide coating along the tube in light water reactors. This unique multimodal imaging and microanalysis effort gives a great example of how advanced correlative imaging and spectroscopy can be used to assess chemical and microstructural evolution in functional coatings employed in extreme environments to advance coating material applications in irradiation conditions relevant to nuclear science and processing.

associated with the alumina and chromium oxide layer in the irradiated sample from the lower core region. Cr is not a component of the powder pack used to create the aluminide coating, and its distribution in the coating is a by-product of the coating process. Additionally, Cr prohibits the β-NiAl phase transformation and reduces coating degradation [65–69]. The depth profile of the enriched $^6Li^-$ m/z^- 6.0157 tracks that C^3H^- m/z^- 15.0165, indicating similar diffusivities. The appearance of $^{195}Pt^-$ m/z^- 194.9725 arises from the SEM-FIB welding process, this signal is not inherent of the cladding material. AlO^- m/z^- 42.9794 and C^- m/z^- 12.000 are selected to illustrate the chemical makeup of alumina and carbon components in the cladding. The abundances of tritium and lithium related ions are much lower in the irradiated middle cladding (Fig. 4c), further illustrating that the likely path of lithium transport from the pellet to the cladding could be along the tube (Fig. S1) and via the gap at the end of the internal target components.

Appendix A. Supplementary data

Supplementary data to this article can be found online at https://doi.org/10.1016/j.jmrt.2021.06.066.

REFERENCES

[1] Stoloff NS. Iron aluminides: present status and future prospects. Mater Sci Eng, A 1998;258(1):1−14.

[2] Wang D, Shi Z. Aluminizing and oxidation treatment of $^1Cr_{18}Ni_9$ stainless steel. Appl Surf Sci 2004;227(1−4):255−60.

[3] Thiem PG, Chornyi A, Smirnov IV, Krüger M. Comparison of microstructure and adhesion strength of plasma, flame and high velocity oxy-fuel sprayed coatings from an iron aluminide powder. Surf Coating Technol 2017;324:498−508.

[4] Glasbrenner H, Perujo A, Serra E. Hydrogen permeation behaviour of hot-dip aluminized MANET steel. Fusion Technol 1995;28(3P2):1159−64.

[5] Lopes NIdA, Freire NHJ, Resende PD, Silva JD, Santos LdA, Béclin F, et al. ToF-SIMS characterization of nanostructured ZrO2 coatings applied to near equiatomic Ni-Ti alloy. Mater Res 2019;22.

[6] Liu W-j, Wang Y, Ge H-b, Li L, Ding Y, Meng L-g, et al. Microstructure evolution and corrosion behavior of Fe-Al-based intermetallic aluminide coatings under acidic condition. Trans Nonferrous Metals Soc China 2018;28(10):2028−43.

[7] Ahledel N, Schulz R, Gariepy M, Hermawan H, Alamdari H. Electrochemical corrosion behavior of Fe₃Al/TiC and Fe₃Al-Cr/TiC coatings prepared by HVOF in NaCl solution. Metals 2019;9(4):437.

[8] Senderowski C, Cinca N, Dosta S, Cano IG, Guilemany JM. The effect of hot treatment on composition and microstructure of HVOF iron aluminide coatings in Na₂SO₄ molten salts. J Therm Spray Technol 2019;28(7):1492−510.

[9] Mohammadi PO, Raiszadeh R, Shahverdi H. Formation of iron aluminide coatings on plain carbon steel by TIG process. Int J Adv Manuf Technol 2018;96(5):1655−63.

[10] Dutta RS, Bhandari S, Chakravarthy Y, Vishwanadh B, Singh K, Dey GK. Development of aluminide coatings on Ni-Cr-Fe based superalloy 690 substrates for high temperature applications using atmospheric plasma spraying technique. Mater Today: Proceedings 2016;3(9, Part B):3018−24.

[11] Majumdar S, Paul B, Kain V, Dey GK. Formation of Al₂O₃/Fe-Al layers on SS 316 surface by pack aluminizing and heat treatment. Mater Chem Phys 2017;190:31−7.

[12] Mohammadi PO, raiszadeh r, Shahverdi H. Hot corrosion properties of iron aluminide coatings produced via a two stages process on plain carbon steel. Metallurgical Engineering 2017;20(2):109−20.

[13] Nová K, Novák P, Průša F, Kopeček J, Čech J. Synthesis of intermetallics in Fe-Al-Si system by mechanical alloying. Metals 2018;9(1):20.

[14] Zamanzade M, Barnoush A, Motz C. A review on the properties of iron aluminide intermetallics. Crystals 2016;6(1):10.

[15] Palm M, Stein F, Dehm G. Iron aluminides. Annu Rev Mater Res 2019;49(1):297−326.

[16] Zuhailawati H, Fauzi MNA. Mechanical properties of iron aluminides intermetallic alloy with molybdenum addition. AIP Conference Proceedings 2010;1217(1):510−4.

[17] Morgiel J, Zagula-Yavorska M, Zubko M, Romanowska J. SEM/TEM investigation of aluminide coating Co-doped with Pt and Hf deposited on inconel 625. Materials 2018;11(6):898.

[18] Yang HG, Zhan Q, Zhao WW, Yuan XM, Hu Y, Han ZB. Study of an iron-aluminide and alumina tritium barrier coating. J Nucl Mater 2011;417(1):1237−40.

[19] Rösner H, Molénat G, Nembach E. In situ TEM observations of dislocation processes in iron-aluminides with 25 and 30 at.% aluminium. Mater Sci Eng, A 1996;216(1):169−77.

[20] Martinez M, Viguier B, Maugis P, Lacaze J. Relation between composition, microstructure and oxidation in iron aluminides. Intermetallics 2006;14(10):1214−20.

[21] Keller RR, Wowchak AM, Angelo JE, Kuznia JN, Cohen PI, Gerberich WW. Growth and characterization of iron aluminide films on compound semiconductors. J Electron Mater 1991;20(4):319−24.

[22] Muñoz-Morris MA, Garcia Oca C, Morris DG. An analysis of strengthening mechanisms in a mechanically alloyed, oxide dispersion strengthened iron aluminide intermetallic. Acta Mater 2002;50(11):2825−36.

[23] Wright RN, Anderson MT, Wright JK. Microstructure and properties of an oxide dispersion-strengthened iron aluminide. Mater Sci Eng, A 1998;258(1):285−90.

[24] Olszówka-myalska A, Maziarz W. Microstructural analysis of iron aluminide formed by self-propagating high-temperature synthesis mechanism in aluminium matrix composite. J Microsc 2006;224(1):1−3.

[25] Sadeghi E, Markocsan N, Joshi S. Advances in corrosion-resistant thermal spray coatings for renewable energy power plants: Part II—effect of environment and outlook. J Therm Spray Technol 2019;28(8):1789−850.

[26] Zhu Z, Shutthanandan V, Engelhard M. An investigation of hydrogen depth profiling using ToF-SIMS. Surf Interface Anal 2012;44(2):232−7.

[27] Zhu Z, Shutthanandan V. Are cluster ion analysis beams good choices for hydrogen depth profiling using time-of-flight secondary ion mass spectrometry? Surf Interface Anal 2012;44(1):89−93.

[28] Jiang W, Spurgeon SR, Zhu Z, Yu X, Kruska K, Wang T, et al. Chemical imaging and diffusion of hydrogen and lithium in lithium aluminate. J Nucl Mater 2018;511:1−10.

[29] Zhang SD, Wu J, Qi WB, Wang JQ. Effect of porosity defects on the long-term corrosion behaviour of Fe-based amorphous alloy coated mild steel. Corrosion Sci 2016;110:57–70.

[30] Wu J, Zhang SD, Sun WH, Gao Y, Wang JQ. Enhanced corrosion resistance in Fe-based amorphous coatings through eliminating Cr-depleted zones. Corrosion Sci 2018;136:161–73.

[31] Burns KA, Love EF, Thornhill CK. Description of the tritium-producing burnable absorber rod for the commercial light water reactor. Richland, WA (United States): Pacific Northwest National Lab. (PNNL); 2012 [p. Medium: ED; Size: PDFN].

[32] Roberts RM, Elleman TS, H.P III, Verghese K. Hydrogen permeability of sintered aluminum oxide. J Am Ceram Soc 1979;62(9-10):495–9.

[33] Roberts R, Ellemen T, Palmour H, Verghese K. Hydrogen permeability of sintered aluminum oxide. J Am Ceram Soc 1979;62.

[34] Hollenberg G, Bagaassen L, Kurosky R, Tonn D, Carty W. Scale-up of lithium aluminate pellet manufacturing with a flowable powder. In: Environmental issues and waste management technologies in the ceramic and nuclear industries IX; 2006. p. 41–54.

[35] Jiang W, Spurgeon SR, Matthews BE, Battu AK, China S, Varga T, et al. Carbonaceous deposits on aluminide coatings in tritium-producing assemblies. Nuclear Materials and Energy 2020;25:100797.

[36] Wojnárovits L. Radiation chemistry. In: Vértes A, Nagy S, Klencsár Z, Lovas RG, Rösch F, editors. Handbook of nuclear chemistry. Boston, MA: Springer US; 2011. p. 1263–331.

[37] Foreman MRSJ. An introduction to serious nuclear accident chemistry. Cogent Chemistry 2015;1(1):1049111.

[38] Tietze S, Foreman MRS, Ekberg CH. Formation of organic iodides from containment paint ingredients caused by gamma irradiation. J Nucl Sci Technol 2013;50(7):689–94.

[39] Song KC, Park GI, Lee JW, Park JJ, Yang MS. Fractional release behavior of volatile and semivolatile fission products during a voloxidation and OREOX treatment of spent PWR fuel. Nucl Technol 2008;162(2):158–68.

[40] Li C, Habler G, Baldwin LC, Abart R. An improved FIB sample preparation technique for site-specific plan-view specimens: a new cutting geometry. Ultramicroscopy 2018;184:310–7.

[41] Langford RM, Clinton C. In situ lift-out using a FIB-SEM system. Micron 2004;35(7):607–11.

[42] Tomus D, Ng HP. In situ lift-out dedicated techniques using FIB–SEM system for TEM specimen preparation. Micron 2013;44:115–9.

[43] E.R.-C.f.M.a.S.w. Electrons FEI Helios NanoLab 400SFIB-SEM. Journal of Large-Scale Research Facilities 2016;2:1–4.

[44] Grehl T, Möllers R, Niehuis E. Low energy dual beam depth profiling: influence of sputter and analysis beam parameters on profile performance using TOF-SIMS. Appl Surf Sci 2003;203–204:277–80.

[45] Engkvist J, Bexell U, Grehk TM, Olsson M. ToF-SIMS depth profiling of alumina scales formed on a FeCrAl high-temperature alloy. Appl Surf Sci 2004;231–232:850–3.

[46] Yunin PA, Drozdov YN, Drozdov MN. A new approach to express ToF SIMS depth profiling. Surf Interface Anal 2015;47(7):771–6.

[47] Holzer S, Krivec S, Kayser S, Zakel J, Hutter H. Large O_2 cluster ions as sputter beam for ToF-SIMS depth profiling of alkali metals in thin SiO2 films. Anal Chem 2017;89(4):2377–82.

[48] Seah MP, Mulcahy CPA, Biswas S. Nonlinearities in depth profiling nanometer layers. J Vac Sci Technol B 2010;28(6):1215–21.

[49] Hua X, Szymanski C, Wang Z, Zhou Y, Ma X, Yu J, et al. Chemical imaging of molecular changes in a hydrated single cell by dynamic secondary ion mass spectrometry and super-resolution microscopy. Integrative biology : quantitative biosciences from nano to macro 2016;8(5):635–44.

[50] Li J-T, Światowska J, Maurice V, Seyeux A, Huang L, Sun S-G, et al. XPS and ToF-SIMS study of electrode processes on Sn–Ni alloy anodes for Li-ion batteries. J Phys Chem C 2011;115(14):7012–8.

[51] Collinet-Fressancourt M, Nuns N, Bellayer S, Traisnel M. Characterization by TEM and ToF-SIMS of the oxide layer formed during anaphoretic paint electrodeposition on Al-alloys. Appl Surf Sci 2013;277:186–91.

[52] Visbal H, Nagashima K, Hirao K. Surface analysis of three aluminum foils and relation to hydrogen generation capability. Kor J Chem Eng 2016;33(4):1255–60.

[53] Kanyal SS, Jensen DS, Zhu Z, Linford MR. Al2O3 e-beam evaporated onto silicon (100)/SiO2 by ToF-SIMS. Surf Sci Spectra 2015;22(2):7–13.

[54] Agüero A, Gutiérrez M, González V. Deposition process of slurry iron aluminide coatings. Mater A T High Temp 2008;25(4):257–65.

[55] Okai T, Takashima Y. Tritium concentrations in atmospheric water vapor, hydrogen and hydrocarbons in Fukuoka. Int J Radiat Appl Instrum Appl Radiat Isot 1991;42(4):389–93.

[56] Yang K, Gant PL. Reactions initiated by β decay of tritium. II. The tritium-ethylene system. J Chem Phys 1959;31(6):1589–94.

[57] Imaizumi H. Effect of tritium on hydrogen isotope exchange reaction in a heterogeneous system. J Radioanal Nucl Chem 1994;177(2):229–41.

[58] O'hira S, Nakamura H, Okuno K, Taylor DJ, Sherman RH. Beta-decay induced reaction studies of tritium by laser Raman spectroscopy — T2-CO system —. Fusion Technol 1995;28(3P2):1239–43.

[59] Lewis RJ, Telle HH, Bornschein B, Kazachenko O, Kernert N, Sturm M. Dynamic Raman spectroscopy of hydrogen isotopomer mixtures in-line at TILO. Laser Phys Lett 2008;5(7):522–31.

[60] Sheludiakov S, Ahokas J, Järvinen J, Lehtonen L, Vainio O, Vasiliev S, et al. ESR study of atomic hydrogen and tritium in solid T2 and T2:H2 matrices below 1 K. Phys Chem Chem Phys 2017;19(4):2834–42.

[61] Uda T, Okuno K, Naruse Y. Hydrogen isotope exchange reaction rate in tritium and methane mixed gas. J Radioanal Nucl Chem 1992;159(1):145–54.

[62] Svec HJ, Anderson AR. The absolute abundance of the lithium isotopes in natural sources. Geochem Cosmochim Acta 1965;29(6):633–41.

[63] Pacific Northwest National Laboratory. In: Bagaasen L, editor. Procurement doment review form - production pellet analytical chemistry report, milestone 5.3. Richland, WA (United States): Pacific Northwest National Lab. (PNNL); 2003.

[64] Duan YH, Sorescu DC, Jiang WL, Senor DJ. Theoretical study of the electronic, thermodynamic, and thermo-conductive properties of gamma-LiAlO2 with Li-6 isotope substitutions for tritium production. J Nucl Mater 2020;530:10.

[65] J S, Wu Duoli, Fan Qixiang, Gong Jun, Sun Chao. Hot corrosion behavior of a Cr-modified aluminide coating on a Ni-based superalloy. Acta Metall Sin 2014;27(4):627–34.

[66] Klöwer J. High temperature corrosion behaviour of iron aluminides and iron-aluminium-chromium alloys. Mater Corros 1996;47(12):685–94.

[67] Pint BA. High temperature corrosion behavior of iron aluminide alloys and coatings. 2001. p. v. United States.

[68] Houngninou C, Chevalier S, Larpin JP. High-temperature-oxidation behavior of iron–aluminide diffusion coatings. Oxid Metals 2006;65(5/6):409–39.

[69] Novák P, Nová K. Oxidation behavior of Fe-Al, Fe-Si and Fe-Al-Si intermetallics. Materials 2019;12(11):1748 (Basel).